frontiers | Frontiers in Chemistry

TYPE Original Research
PUBLISHED 30 September 2022
DOI 10.3389/fchem.2022.1020538

OPEN ACCESS

EDITED BY
Weichun Huang,
Nantong University, China

REVIEWED BY
Ye Zhang,
University of South China, China
Lingfeng Gao,
Hangzhou Normal University, China
Mengke Wang,
Nantong University, China

*CORRESPONDENCE
Xitian Zhang,
xtzhangzhang@hotmail.com
LiLi Wu,
wll790107@hotmail.com

†These authors have contributed equally to this work

SPECIALTY SECTION
This article was submitted to Nanoscience, a section of the journal Frontiers in Chemistry

RECEIVED 16 August 2022
ACCEPTED 12 September 2022
PUBLISHED 30 September 2022

CITATION
Zhang W, Zhang W, Yao J, Lu H, Zhang X and Wu L (2022), Mixed-dimensional $V_2CT_x/Ti_3C_2T_x$ composite interlayer to boost electrochemical performance of Li-S batteries.
Front. Chem. 10:1020538.
doi: 10.3389/fchem.2022.1020538

Mixed-dimensional $V_2CT_x/Ti_3C_2T_x$ composite interlayer to boost electrochemical performance of Li-S batteries

Weiqi Zhang†, Wenchao Zhang†, Jing Yao, Huiqing Lu, Xitian Zhang* and LiLi Wu*

Key Laboratory for Photonic and Electronic Bandgap Materials, Ministry of Education, School of Physics and Electronic Engineering, Harbin Normal University, Harbin, China

Abstract: A mixed-dimensional $V_2CT_x/Ti_3C_2T_x$ composite interlayer was successfully prepared to tackle severe polysulfide (LiPS) shuttling and sluggish sulfur redox kinetics for high-performance lithium–sulfur batteries. In the unique nanoarchitecture, two-dimensional $Ti_3C_2T_x$ nanosheets served as a stable skeleton with superb electronic conductivity, good mechanical strength, and high polysulfide adsorption, whereas one-dimensional V_2CT_x nanorods played a crucial role in chemisorbing LiPSs and catalyzing the conversion of LiPSs due to their high polarity and electrocatalysis. With the synergistic effect of V_2CT_x and $Ti_3C_2T_x$ composite nanostructures, the cells with the mixed-dimensional $V_2CT_x/Ti_3C_2T_x$ composite interlayer showed an impressive long-term cycling stability and small capacity decay rate of 0.062% per cycle over 600 cycles at 1 C and exhibited an outstanding rate capability of 935.3 $mAh{\cdot}g^{-1}$ at 2 C.

KEYWORDS

polysulfides, sulfur redox kinetics, $V_2CT_x/Ti_3C_2T_x$, separator, shuttling, lithium–sulfur batteries

Introduction

Lithium–sulfur batteries (LSBs) have been regarded as one of the most promising next-generation high-energy storage devices. This is because of their advantages of possessing high energy density (2,600 $Wh{\cdot}kg^{-1}$) and being low cost and environmentally friendly (Chung et al., 2018; Ye et al., 2020; Xia et al., 2021). However, the notorious shuttle effect of lithium polysulfides (LiPSs) leads to the loss of active materials, the sluggish LiPS redox kinetics, and the inferior cycling performance. These could limit the specific capacity and cycling lifetime of LSBs (Chen et al., 2019; Tian et al., 2020).

It is important that the severe shuttle effect and sluggish LiPS redox kinetics are overcome to obtain high electrochemical performance of LSBs. Among the effective strategies, the high-performance interlayers between the cathode and separator are proposed. Among the various materials, the carbon-based materials are extensively

applied to prepare the interlayer because they have excellent electrical conductivity (Ma et al., 2020; Wei et al., 2020; Yu et al., 2020). However, the weak interaction between nonpolar carbon materials and LiPSs is difficult to block the diffusion of LiPSs to Li metal anode. Therefore, some polar materials, such as metal oxides (Guo et al., 2019; Li et al., 2020), sulfides (Paolella et al., 2018; Yao et al., 2018), nitrides (Yao et al., 2020), and metal–organic frameworks (Wu et al., 2019), are used to prepare interlayers to further chemically anchor LiPSs. Although they can well immobilize the LiPSs and hinder the shuttle effect, their poor electrical conductivity slows down the multistep redox reactions of sulfur (S) species. Recent research studies showed that a catalyst could make the conversion of LiPSs become fast and shorten the residence time of LiPSs in an electrolyte (Song et al., 2019; Zhang et al., 2020). Therefore, if the incorporated interlayers have an excellent electrical conductivity and could anchor the LiPSs as well as catalyze the LiPS conversion, the slow LiPS redox kinetics and the notorious shuttle effect of the LiPSs could be effectively resolved. Thus, the high-performance interlayer was constructed with a rational design. As a representative, post-graphene two-dimensional (2D) black phosphorus (BP) (Hu et al., 2020) and MXenes (Naguib et al., 2011; Gao et al., 2020; Gao et al., 2021a; Gao et al., 2021b; Zhang et al., 2021; Gao et al., 2022a; Gao et al., 2022b; Cao et al., 2022) have attracted tremendous attention since 2011, due to the layered structure and excellent physicochemical properties. $Ti_3C_2T_x$, a typical MXene material, has been widely used as interlayer materials in LSBs (Ghidiu et al., 2014; Liang et al., 2015; Song et al., 2020). Compared with the carbon-/metal-based materials, $Ti_3C_2T_x$ possesses good conductivity for electron transport and high mechanical properties for structure stability. Nevertheless, 2D $Ti_3C_2T_x$ nanosheets tend to aggregate, which will lead to a decrease in active sites for trapping and catalyzing LiPSs, and slow down the ion transport as well (Qiu et al., 2020). One-dimensional (1D) V_2CT_x nanostructures has been recently explored, which possesses the advantages of strong adsorption to LiPSs and catalytic properties (Wu et al., 2020; Zhang et al., 2022). Therefore, mixed-dimensional $V_2CT_x/Ti_3C_2T_x$ nanostructures together as interlayers will achieve high electrochemical performance for LSBs.

Herein, we construct a mixed-dimensional $V_2CT_x/Ti_3C_2T_x$ composite interlayer on separators for LSBs. It can anchor LiPSs by strong chemisorption and accelerate their redox kinetics under the existence of V_2CT_x catalyst. Based on the unique structure, the LSBs achieve an excellent rate capacity of 935.3 $mAh{\cdot}g^{-1}$ at 2 C. Also, a low-capacity rate decay of 0.062% is obtained after 600 cycles at 1 C. These results illustrate that the incorporation of the multifunctional interlayer is a direct and effective method to achieve high electrochemical performance for LSBs.

Materials and methods

Preparation of mixed-dimensional $V_2CT_x/Ti_3C_2T_x$ interlayers

One-dimensional V_2CT_x nanorods and two-dimensional $Ti_3C_2T_x$ nanosheets were synthesized based on the previous reports (Qiu et al., 2020; Zhang et al., 2022). The suspensions of 1D V_2CT_x nanorods and 2D $Ti_3C_2T_x$ nanosheets were mixed at a mass ratio of 2:8. Then, saturated LiCl solution was added to the resultant mixed solution and stirred, which led to the mixed $V_2CT_x/Ti_3C_2T_x$ nanostructures settled at the bottom of the container by negatively charge-induced self-assembly (Ghidiu et al., 2014; Naguib et al., 2015). Then, the sediment was washed to remove needless salt. Finally, the $V_2CT_x/Ti_3C_2T_x$ powder was obtained by vacuum-drying. Subsequently, $V_2CT_x/Ti_3C_2T_x$ and PVDF were dissolved in NMP solution at a mass ratio of 9:1, and then the mixed solution was filtered on a Celgard separator (PP) under vacuum. The obtained thin film is called the mixed-dimensional $V_2CT_x/Ti_3C_2T_x$ composite interlayer (the corresponding separator is labelled as $V_2CT_x/Ti_3C_2T_x$-PP). The V_2CT_x and $Ti_3C_2T_x$ interlayers were prepared using the same procedure. The corresponding separators are labelled as V_2CT_x-PP and $Ti_3C_2T_x$-PP, respectively.

Li_2S_6 adsorption experiment

Li_2S_6 solution of 0.01 M was prepared by the chemical reaction of Li_2S and S at a molar ratio of 1:5 in a 1, 3-dioxolane (DOL) and 1, 2-dimethoxyethane (DME) mixture (1:1 v/v) at 60°C. A volume of 12 mg of $Ti_3C_2T_x$ and $V_2CT_x/Ti_3C_2T_x$ was added into 1 ml of Li_2S_6 solution, and then, the solutions were rested for adsorption.

Assembly of symmetric cells

$Ti_3C_2T_x$ and $V_2CT_x/Ti_3C_2T_x$ (w/w 2:8) were dissolved in alcohol solution. The resulting solutions were dripped onto the carbon paper (CP) with a diameter of 15 mm (labelled as $Ti_3C_2T_x$-CP and $V_2CT_x/Ti_3C_2T_x$-CP). Both mass loadings were ~0.50 $mg{\cdot}cm^{-2}$. The 2025-type coin cells with two $Ti_3C_2T_x$-CP or $V_2CT_x/Ti_3C_2T_x$-CP electrodes as the anode and cathode were assembled, using PP and 0.1 M of Li_2S_6 as the electrolyte.

Nucleation of Li_2S on $Ti_3C_2T_x$ and $V_2CT_x/Ti_3C_2T_x$

First, 0.25 M of Li_2S_8 solution was obtained by dissolving S and Li_2S at a molar ratio of 7:1 in a tetraglyme solvent at 60°C

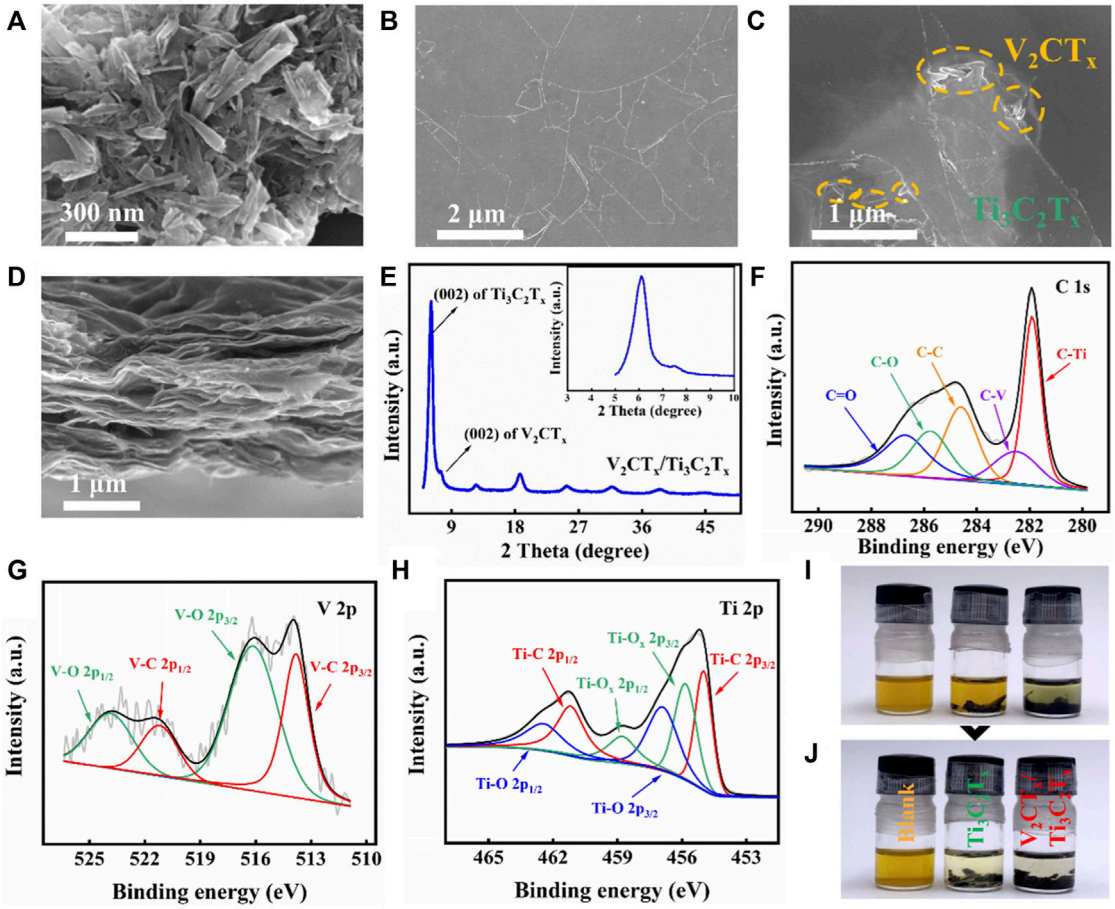

FIGURE 1
SEM images of **(A)** V_2CT_x nanorods, **(B)** $Ti_3C_2T_x$ nanosheets, and **(C)** $V_2CT_x/Ti_3C_2T_x$ composite interlayer. **(D)** Cross-sectional SEM image and **(E)** XRD pattern of the $V_2CT_x/Ti_3C_2T_x$ composite interlayer. High-resolution XPS spectra of **(F)** C1s, **(G)** V 2p, and **(H)** Ti 2p of the $V_2CT_x/Ti_3C_2T_x$ composite interlayer. Visualized experiment of Li_2S_6: **(I)** initial states and **(J)** final states after 5 h.

overnight. Following this, $Ti_3C_2T_x$ and $V_2CT_x/Ti_3C_2T_x$ were dissolved in alcohol solution to obtain uniform suspensions by ultrasound, which were dripped on CPs (10 mm diameter) and dried at 60°C to obtain electrodes. The coin cell was composed of $Ti_3C_2T_x$-CP or $V_2CT_x/Ti_3C_2T_x$-CP cathode, lithium anode, and PP. The Li_2S_8 electrolyte of 0.25 M was used on the cathode side, and the standard electrolyte was used on the anode side. Then, the cells were galvanostatically discharged to 2.06 V at 0.112 mA and then kept at 2.05 V. Also, Li_2S nucleated and grew until the current of 10^{-2} A was reached.

Material characterizations and electrochemical analyses

The morphology of mixed-dimensional $V_2CT_x/Ti_3C_2T_x$ composite interlayers were observed using scanning electron microscopy (SEM) (SU70, Japan). The X-ray diffraction (XRD) measurement was recorded using a Rigaku D/max2600 X-ray diffractometer. The cathode is a mixture of Ketjen black/sulfur, super-P, and PVDF at a mass ratio of 8:1:1. The diameter of the cathode was about 13 mm, and the loading of S was ~1 mg·cm^{-2}. The coin cells were assembled with KB/S cathode, Li anode, and PP with $Ti_3C_2T_x$-PP, $V_2CT_x/Ti_3C_2T_x$-PP, or V_2CT_x-PP, respectively. The electrolyte consisted of 1.0 M lithium bis-trifluoromethane sulfonimide (LiTFSI), 2% $LiNO_3$ additives, and a mixture of DOL/DME (volume ratio = 1:1). The galvanostatic charge–discharge (GCD) profile of the assembled cells was tested at 0.5 C in the voltage range of 1.7–2.6 V using the LAND cell testing system. The electrochemical impedance spectra (EIS) and cyclic voltammograms (CV) were carried out using an electrochemical workstation (VMP3). X-ray photoelectron spectroscopy (XPS) was conducted by applying ESCALAB 250XI.

Results and discussion

SEM images of 1D V_2CT_x nanorods and 2D $Ti_3C_2T_x$ nanosheets are shown in Figures 1A,B. The length of V_2CT_x nanorods is about 230 nm, while the diameter is tens of nanometers. Also, the size of irregular 2D $Ti_3C_2T_x$ nanosheets is a few micrometers. Furthermore, the top-view SEM image of the mixed-dimensional $V_2CT_x/Ti_3C_2T_x$ composite interlayer is presented in Figure 1C. The trace amount of V_2CT_x nanorods can be seen on the top surface of the composite interlayer. On the other hand, the cross-sectional SEM image of the $V_2CT_x/Ti_3C_2T_x$ composite interlayer shows that V_2CT_x and $Ti_3C_2T_x$ are superimposed on each other, forming a well-arranged layered stacking structure (Figure 1D). XRD of the $V_2CT_x/Ti_3C_2T_x$ composite interlayer was carried out to characterize the crystalline structure, as shown in Figure 1E. The two diffraction peaks at 6.1 and 7.45° correspond to the (002) crystal plane of 2D $Ti_3C_2T_x$ nanosheets and 1D V_2CT_x nanorods, respectively (Li et al., 2017; Zhang et al., 2022). In contrast, the (002) diffraction peak intensity of V_2CT_x is weaker, due to the low content of V_2CT_x. The XRD pattern proves that V_2CT_x and $Ti_3C_2T_x$ were successfully synthesized. The composition of the $V_2CT_x/Ti_3C_2T_x$ composite interlayer was further confirmed by XPS analysis (Li et al., 2017; Zhang et al., 2022). A high-resolution XPS spectrum of C 1s in the $V_2CT_x/Ti_3C_2T_x$ composite interlayer is shown in Figure 1F. C-V and C-Ti bonds were observed. Meanwhile, the corresponding V-C and Ti-C bonds can also be found in the high-resolution XPS spectra of V 2p and Ti 2p in V_2CT_x and $Ti_3C_2T_x$, respectively, further proving that the composite interlayer is composed of V_2CT_x and $Ti_3C_2T_x$ (Figures 1G,H). The LiPS adsorption behavior of $V_2CT_x/Ti_3C_2T_x$ composite materials was surveyed by visualized adsorption tests, as shown in Figures 1I,J. $Ti_3C_2T_x$ was used as the control sample. Figure 1I shows the initial states of different samples placed in Li_2S_6 solutions. In Figure 1J, the solvent colors with both $Ti_3C_2T_x$ and $V_2CT_x/Ti_3C_2T_x$ composite materials undergo a significant change after resting for 5 h. The solution including $Ti_3C_2T_x$ materials changes only lighter in color. However, the solution including $V_2CT_x/Ti_3C_2T_x$ composite materials become almost colorless. These findings demonstrate the strong chemical adsorption of $V_2CT_x/Ti_3C_2T_x$ composite materials to LiPSs compared with $Ti_3C_2T_x$.

The mixed-dimensional interlayer with more active sites and stronger catalytic capacity can facilitate the solid–liquid–solid transformations of the S species. At the first stage of LiPS conversions in LSBs, S undergoes solid–liquid phase transformation to high-order LiPSs and then liquid–liquid conversion to low-order LiPSs. Rapid liquid–liquid phase conversions will reduce LiPS accumulation in the electrolyte, which is conductive to ion transport. To investigate the effect of interlayers on the conversions of LiPSs in a liquid–liquid phase, the CV curves of $V_2CT_x/Ti_3C_2T_x$-CP and $Ti_3C_2T_x$-CP symmetric cells were measured, as shown in Figure 2A. The current response of the CP symmetric cell without Li_2S_6 is almost in line. It can be seen from Figure 2A that the current response of $V_2CT_x/Ti_3C_2T_x$-CP symmetric cells with Li_2S_6 is the largest among the $Ti_3C_2T_x$-CP and CP cells, indicating that $V_2CT_x/Ti_3C_2T_x$ composite materials accelerate the liquid–liquid conversion of LiPSs, make the liquid phase LiPS conversion become more thorough, and boost the LiPS redox kinetics. At the same time, the accumulation of LiPSs in the electrolyte will also be greatly reduced. This is due to the rapid conversion of liquid LiPSs. It is beneficial to suppress the shuttle effect. Figure 2B shows the EIS curves of symmetric cells. The smallest semicircle diameter of the $V_2CT_x/Ti_3C_2T_x$-CP symmetric cell implies the smallest charge transfer resistance (R_{ct}), thus confirming the rapid electron and ion transportation at the interface between $V_2CT_x/Ti_3C_2T_x$ composite materials and S species. Kinetics of Li_2S precipitation in LSBs is another significant factor for high-performance LSBs. This is due to the fact that 75% of the capacity originates from the Li_2S deposition during discharge. Therefore, Li_2S nucleation tests were carried out. The constant-voltage discharge curves at 2.05 V are shown in Figures 2C,D. Obviously, the $V_2CT_x/Ti_3C_2T_x$-CP electrode demonstrates the earlier Li_2S deposition compared with $Ti_3C_2T_x$-CP electrodes, indicating that the $V_2CT_x/Ti_3C_2T_x$-CP electrode has the greater catalytic ability, and accelerates the conversion of LiPSs to Li_2S. The Li_2S precipitation capacity on $Ti_3C_2T_x$-CP and $V_2CT_x/Ti_3C_2T_x$-CP electrodes were calculated by the integral of current vs. time, corresponding to 540 and 595 $mAh{\cdot}g^{-1}$, respectively. The precipitation capacity of the $V_2CT_x/Ti_3C_2T_x$-CP electrode becomes higher, implying that the faster LiPS conversion is achieved. The PP, $Ti_3C_2T_x$-PP, and $V_2CT_x/Ti_3C_2T_x$-PP cells were assembled to assess the effect of PP, $Ti_3C_2T_x$-PP, and $V_2CT_x/Ti_3C_2T_x$-PP on the electrochemical performance of LSBs. Figure 2E shows the CV profiles of PP, $Ti_3C_2T_x$-PP, and $V_2CT_x/Ti_3C_2T_x$-PP cells at a scan rate of 0.1 $mV{\cdot}s^{-1}$. Two reduction peaks for three cells can be seen and be attributed to the two reduction processes of S_8 to LiPSs (Li_2S_x, $4 \le x \le 8$) and Li_2S_4 to Li_2S_2/Li_2S, respectively. Two oxidation peaks correspond to the oxidation process of Li_2S to LiPSs, which are then oxidized to S_8. The CV curve of the $V_2CT_x/Ti_3C_2T_x$-PP cell shows the most intense peak, the lowest electrochemical polarization, and the highest current density, illustrating that the $V_2CT_x/Ti_3C_2T_x$ composite interlayer makes LiPS redox reactions become the fastest among PP and $Ti_3C_2T_x$-PP cells. In addition, Figure 2F also reveals the excellent electrochemical kinetics of the $V_2CT_x/Ti_3C_2T_x$-PP cell from the EIS curve. The results show that the $V_2CT_x/Ti_3C_2T_x$-PP cell has the lowest R_{ct} and excellent charge transfer ability at the electrolyte/electrode interface. This is due to its high ionic and electronic conductivity.

The GCD curves of different cells were measured at 0.5 C, as shown in Figure 3A. The discharge capacities of $V_2CT_x/Ti_3C_2T_x$-PP, $Ti_3C_2T_x$-PP, V_2CT_x-PP, and PP cells are 1,090, 2,

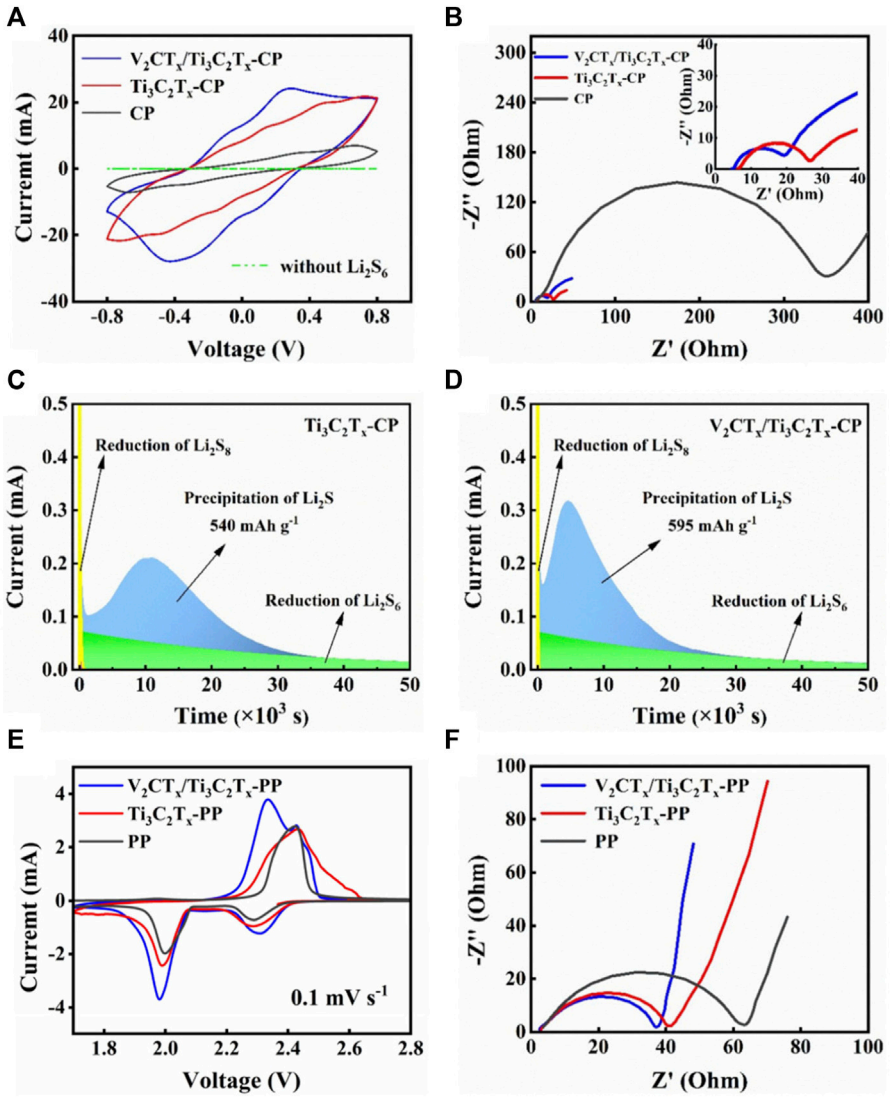

FIGURE 2
(A) CV curves of different symmetric cells under 50 mV·s^{-1} and **(B)** EIS spectra of $V_2CT_x/Ti_3C_2T_x$-CP, $Ti_3C_2T_x$-CP, and CP symmetric cells using Li_2S_6. Current vs. time curves for **(C)** $Ti_3C_2T_x$-CP and **(D)** $V_2CT_x/Ti_3C_2T_x$-CP electrodes. **(E)** CV curves of PP, $Ti_3C_2T_x$-PP, and $V_2CT_x/Ti_3C_2T_x$-PP cells at 0.1 mV·s^{-1}. **(F)** EIS spectra of PP, $Ti_3C_2T_x$-PP, and $V_2CT_x/Ti_3C_2T_x$-PP cells.

977.3, 892.4, and 842.8 mAh·g^{-1}, respectively. In contrast, the $V_2CT_x/Ti_3C_2T_x$-PP cell has the highest specific discharge capacity due to the existence of trace amounts of V_2CT_x. In addition, the polarization overpotential of the $V_2CT_x/Ti_3C_2T_x$-PP cell is only 211 mV, which is significantly smaller than that of other cells and consistent with the results of CV tests. Then, the cycling performance tests of the PP, $Ti_3C_2T_x$-PP, and $V_2CT_x/Ti_3C_2T_x$-PP cells were also performed, as shown in Figure 3B. The $V_2CT_x/Ti_3C_2T_x$-PP cell can still remain at a high discharge capacity of 775.2 mAh·g^{-1} and high capacity retention rate of 71% after 300 cycles. However, the capacity retention rate of $Ti_3C_2T_x$-PP and PP cells are only 69 and 52% after 300 cycles, respectively. Under the rate performance test shown in Figure 3C, the $V_2CT_x/Ti_3C_2T_x$ cell shows excellent rate performance as the current density changes due to the good ionic and electronic conductivity of the $V_2CT_x/Ti_3C_2T_x$ composite interlayer. In Figure 3C, the discharge capacity of the $V_2CT_x/Ti_3C_2T_x$-PP cell is 1,299.2, 1,185.9, 1,061.8, 998.3, and 935.3 mAh·g^{-1} at 0.1, 0.2, 0.5, 1, and 2 C, respectively. Subsequently, the discharge capacity can be restored to the high reversible capacity of 1,151.8 mAh·g^{-1} by reducing to 0.1 C. However, the discharge capacity of $Ti_3C_2T_x$-PP and PP

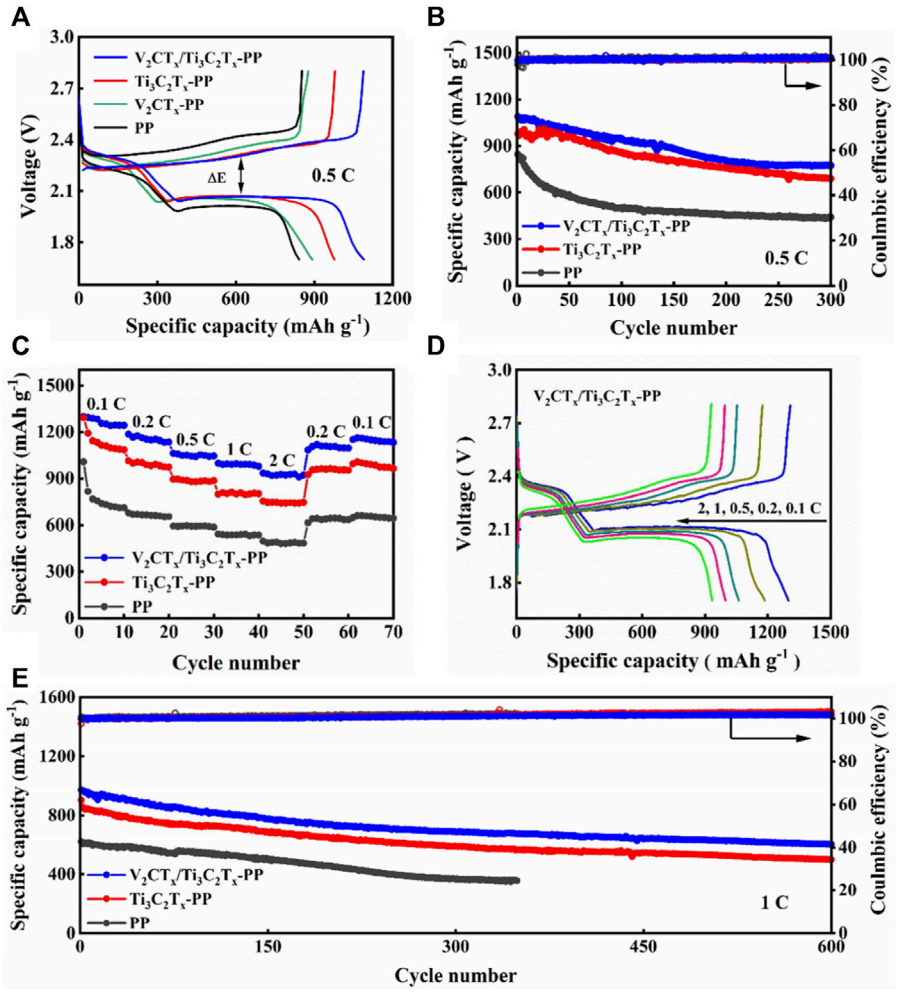

FIGURE 3
(A) GCD curves of $V_2CT_x/Ti_3C_2T_x$-PP, $Ti_3C_2T_x$-PP, V_2CT_x-PP, and PP cells at 0.5 C. **(B)** Cycling performance of $V_2CT_x/Ti_3C_2T_x$-PP, $Ti_3C_2T_x$-PP, and PP cells at 0.5 C. **(C)** Rate performance of $V_2CT_x/Ti_3C_2T_x$-PP, $Ti_3C_2T_x$-PP, and PP cells. **(D)** GCD curves of the $V_2CT_x/Ti_3C_2T_x$-PP cell at current densities of 0.1, 0.2, 0.5, 1, and 2 C. **(E)** Cycling performance of $V_2CT_x/Ti_3C_2T_x$-PP, $Ti_3C_2T_x$-PP, and PP cells at 1 C.

cells is 753.9 and 469.2 mAh·g^{-1} at 2 C, respectively, indicating that the capacity decays faster with the increase in current density. Their reversible capacities correspond to 993 and 647.1 mAh·g^{-1} at 0.1 C, respectively. Figure 3D shows the GCD profiles of the $V_2CT_x/Ti_3C_2T_x$-PP cell. The polarization of the $V_2CT_x/Ti_3C_2T_x$-PP cell is only 123.4 mV at 0.1 C. The excellent rate performance and low polarization of the $V_2CT_x/Ti_3C_2T_x$-PP cell can be attributed to the important role of the mixed-dimensional $V_2CT_x/Ti_3C_2T_x$ composite interlayer in electrical conductivity and chemical anchoring. The cycle stability at a high current density is an important factor to evaluate the performance of LSBs. Therefore, the long cycling stability of different batteries were tested at 1 C. In Figure 3E, the $V_2CT_x/Ti_3C_2T_x$-PP cell has an excellent long-term cycling stability with a high initial capacity of 969.9 mAh·g^{-1} and low capacity decay rate of 0.062% after 600 cycles. In contrast, the $Ti_3C_2T_x$-PP cell has a capacity decay rate of 0.074%. The PP cell is out of service after less than 400 cycles. The $V_2CT_x/Ti_3C_2T_x$ cell demonstrates excellent electrochemical performance and cycle stability. It is also worth noting that the electrochemical performance of the mixed-dimensional $V_2CT_x/Ti_3C_2T_x$ composite interlayer is highly competitive compared with that of the other materials reported (Table 1). In a word, the adsorbed LiPSs on the composite interlayer can quickly obtain electrons and ions at the adsorption sites to continue the redox reactions based on the high conductivity and abundant active sites of $V_2CT_x/Ti_3C_2T_x$. Meanwhile, the catalytic effect of V_2CT_x accelerates the LiPS redox kinetics.

TABLE 1 Comparison of the electrochemical performance between this work and other previously reported works.

Nanostructure	S loading (mg cm^2)	Discharge rate (C)	Final capacity (mAh g^{-1})	Cycle number	Capacity decay per cycle (%)	Reference
$V_2CT_x/Ti_3C_2T_x$-PP	1.0	0.5	775.2	300	0.096	This work
S/$Ti_3C_2T_x$-N	—	0.5	1,104.3	100	0.138	Qi and Zhang, (2022)
Bi-PP	2.5	0.5	650	200	—	Huang et al. (2020a)
V_2CT_x/CNT-PP	1.0	0.5	1008.3	100	0.204	Zhang et al. (2022)
KB/V_2CT_X-PP	1.0	0.2	942	150	0.158	Han et al. (2022)

Conclusion

In conclusion, we construct a mixed-dimensional V_2CT_x/$Ti_3C_2T_x$ composite interlayer to suppress LiPS shuttling and accelerate LiPS redox kinetics. Profiting from the advantages of strong chemisorption of the composite interlayer to LiPSs and catalysis of V_2CT_x, the $V_2CT_x/Ti_3C_2T_x$ cell achieves an excellent rate capacity of 935.3 mAh·g^{-1} at 2 C and low capacity rate decay of 0.062% after 600 cycles at 1 C. Meanwhile, designing a mixed-dimensional composite interlayer can provide a route to develop high-performance LSBs.

Data availability statement

The original contributions presented in the study are included in the article/Supplementary Material. Further inquiries can be directed to the corresponding author/s.

Author contributions

WiZ, WcZ, and JY contributed to the material preparation and characterization. HL contributed to the TEM measurement. XZ and LW conceived the idea and designed the experiments.

Funding

This work was supported by the National Natural Science Foundation of China (52072099) and the Team Program of the Natural Science Foundation of Heilongjiang Province, China (No. TD 2021E005).

Conflict of interest

The authors declare that the research was conducted in the absence of any commercial or financial relationships that could be construed as a potential conflict of interest.

Publisher's note

All claims expressed in this article are solely those of the authors and do not necessarily represent those of their affiliated organizations, or those of the publisher, the editors, and the reviewers. Any product that may be evaluated in this article, or claim that may be made by its manufacturer, is not guaranteed or endorsed by the publisher.

References

Cao, F. C., Zhang, Y., Wang, H. Q., Khan, K., Tareen, A. K., Qian, W. J., et al. (2022). Recent advances in oxidation stable chemistry of 2D MXenes. *Adv. Mater.* 34, 2107554. doi:10.1002/adma.202107554

Chen, L., Yang, W., Liu, J., and Zhou, Y. (2019). Decorating $CoSe_2$ hollow nanospheres on reduced graphene oxide as advanced sulfur host material for performance enhanced lithium-sulfur batteries. *Nano Res.* 12, 2743–2748. doi:10.1007/s12274-019-2508-3

Chung, S. H., Chang, C. H., and Manthiram, A. (2018). Progress on the critical parameters for lithium-sulfur batteries to be practically viable. *Adv. Funct. Mat.* 28, 1801188. doi:10.1002/adfm.201801188

Gao, B., Li, Y. Y., Ma, C. Y., Shu, Y. Q., Wu, G., Chen, B. C., et al. (2022). Ta_4C_3 MXene as a saturable absorber for femtosecond mode-locked fiber lasers. *J. Alloys Compd.* 900, 163529. doi:10.1016/j.jallcom.2021.163529

Gao, L. F., Bao, W. L., Kuklin, A. V., Mei, S., Zhang, H., and Ågren, H. (2021). Hetero-MXenes: Theory, synthesis, and emerging applications. *Adv. Mat.* 33, 2004129. doi:10.1002/adma.202004129

Gao, L. F., Chen, H. L., Kuklin, A. V., Wageh, S., Al-Ghamdi, A. A., Ågren, H., et al. (2022). Optical properties of few-layer Ti_3CN MXene: From experimental observations to theoretical calculations. *ACS Nano* 16, 3059–3069. doi:10.1021/acsnano.1c10577

Gao, L. F., Ma, C. Y., Wei, S. R., Kuklin, A. V., Zhang, H., and Ågren, H. (2021). Applications of few-layer Nb_2C MXene: Narrow-band photodetectors and femtosecond mode-locked fiber lasers. *ACS Nano* 15, 954–965. doi:10.1021/acsnano.0c07608

Gao, L. G., Li, C., Huang, W. C., Mei, S., Lin, H., Ou, Q., et al. (2020). MXene/polymer membranes: Synthesis, properties, and emerging applications. *Chem. Mat.* 32, 1703–1747. doi:10.1021/acs.chemmater.9b04408

Ghidiu, M., Lukatskaya, M. R., Zhao, M. Q., Gogotsi, Y., and Barsoum, M. W. (2014). Conductive two-dimensional titanium carbide 'clay' with high volumetric capacitance. *Nature* 516, 78–81. doi:10.1038/nature13970

Guo, P., Sun, K., Shang, X., Liu, D., Wang, Y., Liu, Q., et al. (2019). Nb_2O_5/RGO nanocomposite modified separators with robust polysulfide traps and catalytic centers for boosting performance of lithium-sulfur batteries. *Small* 15, 1902363. doi:10.1002/smll.201902363

Han, F. F., Jin, Q., Xiao, J. P., Wu, L. L., and Zhang, X. T. (2022). V_2CT_x catalyzes polysulfide conversion to enhance the redox kinetics of Li-S batteries. *Dalton Trans.* 51, 2560–2566. doi:10.1039/d1dt04158d

Hu, H. G., Shi, Z., Khan, K., Cao, R., Liang, W. Y., Tareen, A. K., et al. (2020). Recent advances in doping engineering of black phosphorus. *J. Mat. Chem. A* 8, 5421–5441. doi:10.1039/d0ta00416b

Huang, W. C., Zhu, J., Wang, M. K., Hu, L. P., Tang, Y. F., Shu, Y. Q., et al. (2020). Emerging mono-elemental bismuth nanostructures: Controlled synthesis and their versatile applications. *Adv. Funct. Mat.* 31, 2007584. doi:10.1002/adfm.202007584

Li, L., Zhang, M. Y., Zhang, X. T., and Zhang, Z. G. (2017). New Ti_3C_2 aerogel as promising negative electrode materials for asymmetric supercapacitors. *J. Power Sources* 364, 234–241. doi:10.1016/j.jpowsour.2017.08.029

Li, N., Chen, F., Chen, X. T., Chen, Z. X., Qi, Y., Li, X. D., et al. (2020). A bipolar modified separator using TiO_2 nanosheets anchored on N-doped carbon scaffold for high-performance Li-S batteries. *J. Mater. Sci. Technol.* 55, 152–158. doi:10.1016/j.jmst.2019.09.012

Liang, X., Garsuch, A., and Nazar, L. F. (2015). Sulfur cathodes based on conductive MXene nanosheets for high-performance lithium-sulfur batteries. *Angew. Chem. Int. Ed.* 54, 3907–3911. doi:10.1002/anie.201410174

Ma, Q., Hu, M., Yuan, Y., Pan, Y., Chen, M., Zhang, Y., et al. (2020). Colloidal dispersion of Nb_2O_5/reduced graphene oxide nanocomposites as functional coating layer for polysulfide shuttle suppression and lithium anode protection of Li-S battery. *J. Colloid Interface Sci.* 566, 11–20. doi:10.1016/j.jcis.2020.01.066

Naguib, M., Kurtoglu, M., Presser, V., Lu, J., Niu, J., Heon, M., et al. (2011). Two-dimensional nanocrystals produced by exfoliation of Ti_3AlC_2. *Adv. Mat.* 23, 4248–4253. doi:10.1002/adma.201102306

Naguib, M., Unocic, R. R., Armstrong, B. L., and Nanda, J. (2015). Large-scale delamination of multi-layers transition metal carbides and carbonitrides "MXenes". *Dalton Trans.* 44, 9353–9358. doi:10.1039/c5dt01247c

Paolella, A., Laul, D., Timoshevskii, V., Zhu, W., Marras, S., Bertoni, G., et al. (2018). The role of metal disulfide interlayer in Li-S batteries. *J. Phys. Chem. C* 122, 1014–1023. doi:10.1021/acs.jpcc.7b08719

Qi, K. L., and Zhang, F. (2022). Rational surface engineering of $Ti_3C_2T_x$ MXene for high-performance lithium-sulfur batteries. *Mater. Lett.* 318, 132134. doi:10.1016/j.matlet.2022.132134

Qiu, S. Y., Wang, C., Jiang, Z. X., Zhang, L. S., Gu, L. L., Wang, K. X., et al. (2020). Rational design of MXene@TiO_2 nanoarray enabling dual lithium polysulfide chemisorption towards high-performance lithium-sulfur batteries. *Nanoscale* 12, 16678–16684. doi:10.1039/d0nr03528a

Song, Y., Cai, W., Kong, L., Cai, J., Zhang, Q., and Sun, J. (2019). Rationalizing electrocatalysis of Li-S chemistry by mediator design: Progress and prospects. *Adv. Energy Mat.* 10, 1901075. doi:10.1002/aenm.201901075

Song, Y. Z., Sun, Z. T., Fan, Z. D., Cai, W. L., Shao, Y. L., Sheng, G., et al. (2020). Rational design of porous nitrogen-doped Ti_3C_2 MXene as a multifunctional electrocatalyst for Li-S chemistry. *Nano Energy* 70, 104555. doi:10.1016/j.nanoen.2020.104555

Tian, Y., Li, G., Zhang, Y., Luo, D., Wang, X., Zhao, Y., et al. (2020). Low-bandgap Se-deficient antimony selenide as a multifunctional polysulfide barrier toward high-performance lithium-sulfur batteries. *Adv. Mat.* 32, 1904876. doi:10.1002/adma.201904876

Wei, L., Li, W. L., Zhao, T., Zhang, N. X., Li, L., Wu, F., et al. (2020). Cobalt nanoparticles shielded in N-doped carbon nanotubes for high areal capacity Li-S batteries. *Chem. Commun.* 56, 3007–3010. doi:10.1039/c9cc08218b

Wu, M., He, Y., Wang, L. B., Xia, Q. X., and Zhou, A. G. (2020). Synthesis and electrochemical properties of V_2C MXene by etching in opened/closed environments. *J. Adv. Ceram.* 9, 749–758. doi:10.1007/s40145-020-0411-8

Wu, X., Liu, N., Guan, B., Qiu, Y., Wang, M., Cheng, J., et al. (2019). Redox mediator: A new strategy in designing cathode for prompting redox process of Li-S batteries. *Adv. Sci.* 6, 1900958. doi:10.1002/advs.201900958

Xia, G., Zheng, Z. Q., Ye, J. J., Li, X. T., Biggs, M. J., and Hu, C. (2021). Carbon microspheres with embedded FeP nanoparticles as a cathode electrocatalyst in Li-S batteries. *Chem. Eng. J.* 406, 126823. doi:10.1016/j.cej.2020.126823

Yao, S., Cui, J., Huang, J. Q., Lu, Z., Deng, Y., Chong, W. G., et al. (2018). Novel 2D Sb_2S_3 nanosheet/CNT coupling layer for exceptional polysulfifide recycling performance. *Adv. Energy Mat.* 8, 1700279. doi:10.1002/aenm.201800710

Yao, Y., Wang, H., Yang, H., Zeng, S., Xu, R., Liu, F., et al. (2020). A dual-functional conductive framework embedded with TiN-VN heterostructures for highly efficient polysulfide and lithium regulation toward stable Li-S full batteries. *Adv. Mat.* 32, 1905658. doi:10.1002/adma.201905658

Ye, Z. Q., Jiang, Y., Li, L., Wu, F., and Chen, R. J. (2020). A high-efficiency CoSe electrocatalyst with hierarchical porous polyhedron nanoarchitecture for accelerating polysulfides conversion in Li-S batteries. *Adv. Mat.* 32, 2002168. doi:10.1002/adma.202002168

Yu, B., Chen, D. J., Wang, Z. G., Qi, F., Zhang, X. J., Wang, X. Q., et al. (2020). Mo_2C quantum dots@graphene functionalized separator toward high-current-density lithium metal anodes for ultrastable Li-S batteries. *Chem. Eng. J.* 399, 125837. doi:10.1016/j.cej.2020.125837

Zhang, B., Luo, C., Deng, Y. Q., Huang, Z. J., Zhou, G. M., Lv, W., et al. (2020). Optimized catalytic WS_2 -WO_3 heterostructure design for accelerated polysulfide conversion in lithium-sulfur batteries. *Adv. Energy Mat.* 10, 2000091. doi:10.1002/aenm.202000091

Zhang, W. Q., Jin, Q., Xiao, J. P., Yao, J., and Zhang, X. T. (2022). Rational design of adsorption-catalysis functional separator for highly efficient Li-S batteries. *J. Alloys Compd.* 900, 163414. doi:10.1016/j.jallcom.2021.163414

Zhang, Y., Xu, Y., Gao, L., Liu, X., Fu, Y., Ma, C., et al. (2021). MXene-based mixed-dimensional Schottky heterojunction towards self-powered flexible high-performance photodetector. *Mater. Today Phys.* 21, 100479. doi:10.1016/j.mtphys.2021.100479